SCIENCE CHINA
Information Sciences

• RESEARCH PAPER •

January 2026, Vol. 69, Iss. 1, 112402:1–112402:9
https://doi.org/10.1007/s11432-025-4516-x

# Sliding-controllable on-off states in $MAX_3$-based ($M$ = Mn, Ni; $A$ = Si, Ge; $X$ = S, Se) van der Waals tunnel junctions

Jianing TAN[1], Meng GE[1], Huamin HU[2], Hai LI[1] & Gang OUYANG[1*]

[1]*Key Laboratory of Low-Dimensional Quantum Structures and Quantum Control of Ministry of Education, Hunan Research Center of the Basic Discipline for Quantum Effects and Quantum Technologies, Key Laboratory for Matter Microstructure and Function of Hunan Province, School of Physics and Electronics, Hunan Normal University, Changsha 410081, China*
[2]*School of Materials Science and Engineering, Changsha University of Science and Technology, Changsha 410114, China*

Received 15 March 2025/Revised 18 May 2025/Accepted 8 July 2025/Published online 4 January 2026

**Abstract** Two-dimensional (2D) materials hold remarkable promise for high-density memory applications, yet precise modulation of interface properties in van der Waals (vdW) tunnel junctions remains a critical challenge. In this work, we systematically investigate the interface contact and charge transport properties of $MAX_3$-based vdW tunnel junctions ($M$ = Mn, Ni; $A$ = Si, Ge; $X$ = S, Se). Our findings demonstrate that controlled sliding between atomic layers enables deterministic regulation of both the Schottky barrier height and magnetic moment orientation, driven by layer-dependent charge redistribution at selenium-terminated interfaces. First-principles calculations combined with non-equilibrium Green's function simulations reveal substantial improvements in tunneling resistance ($\sim 6 \times 10^5\%$) and tunneling magnetoresistance ($\sim 10^{10}\%$) achieved through interface engineering. These results provide a general strategy for tailoring quantum transport in 2D vdW heterostructures, offering a versatile platform for reconfigurable memory devices with atomic-scale precision.

**Keywords** vdW tunnel junctions, sliding engineering, interface barrier modulation, transport properties, density functional theory

**Citation** Tan J N, Ge M, Hu H M, et al. Sliding-controllable on-off states in $MAX_3$-based ($M$=Mn, Ni; $A$=Si, Ge; $X$=S, Se) van der Waals tunnel junctions. Sci China Inf Sci, 2026, 69(1): 112402, https://doi.org/10.1007/s11432-025-4516-x

## 1 Introduction

Tunnel junctions are critical components in electronics and spintronics [1–3]. The advent of two-dimensional (2D) van der Waals (vdW) materials has transformed the design of metal-semiconductor (M-S) junctions, offering superior integration, flexibility, and multifunctionality [4–13]. However, controlling the on/off switching in 2D tunnel junctions, such as modulating the Schottky barrier at the M-S interface or manipulating the magnetic moment orientation in 2D magnets, remains a key challenge, leading to high power consumption and limited tunability [14–19]. Energy efficiency, being essential for multifunctional device design and future technological advancement [20–24], has enabled achievements like the large multistate magnetoresistance in $Fe_3GaTe_2$-based multiferroic tunnel junctions [24].

Extensive efforts have focused on tuning the Schottky barrier height (SBH) via chemical doping, electric fields, polarization switching, and strain engineering [25–29]. These approaches often demand high energy input, limiting their practicality for low-power applications. Recently, sliding has emerged as a promising alternative due to its ultra-low energy consumption [30–32]. Studies suggest sliding can also modulate magnetism in 2D magnets [33,34], yet its impact on interface potential and transport properties remains underexplored.

Noticeably, the transition-metal trichalcogenide family $MAX_3$ ($M$ = V, Cr, Mn, Fe, Co, Ni; $A$ = P, Si, Ge, Sn; $X$ = S, Se, Te) combines a shared structural framework with diverse electronic and magnetic properties [35,36], making it an ideal platform for 2D M-S junctions. The structural uniformity ensures seamless interfaces, while the functional diversity enables broad tunability. In this work, we demonstrate that a sliding path in the $MnSiSe_3/ZnPSe_3$ heterostructure effectively modulates both the SBH and magnetic easy-axis orientation, driven by interfacial charge transfer between selenium atomic layers. To ensure generality, we substituted elements in $MnSiSe_3$, generating

* Corresponding author (email: gangouy@hunnu.edu.cn)

© Science China Press 2026 

three additional systems ($NiSiSe_3$, $MnGeSe_3$, and $MnSiS_3$) paired with $ZnPSe_3$, $ZnAsSe_3$, and $ZnPS_3$, respectively. These heterostructures maintain key properties (e.g., high critical temperatures, half-metallicity) with minimal lattice mismatch, confirming the robustness of our approach.

To validate this strategy, we constructed a tunnel junction using $MnSiSe_3/ZnPSe_3$ as electrodes and a $ZnPSe_3$ monolayer as the insulating barrier. This sliding-driven vdW tunnel junction achieves an exceptional tunnel resistance (TR) ratio of $\sim 6 \times 10^5\%$ and a tunneling magnetoresistance (TMR) ratio of $\sim 10^{10}\%$. Comparable performance was observed in $NiSiSe_3/ZnPSe_3$, $MnGeSe_3/ZnAsSe_3$, and $MnSiS_3/ZnPS_3$ junctions. Our work establishes a low-energy method for tailoring Schottky barriers and magnetic moments in $MAX_3$-based vdW systems, offering a versatile platform for next-generation electronics and spintronics.

## 2 Theoretical methods

This study utilizes density functional theory (DFT) for geometrical relaxation and electronic structure calculations, employing the Vienna ab initio simulation package (VASP) with the projector augmented-wave method [37, 38]. A plane-wave cutoff energy of 500 eV is adopted, and a Hubbard $U$ value of 4.0 eV is applied to address the strong correlation effects in Mn 3d electrons [36]. vdW corrections are incorporated using the D3 method [39], and a vacuum layer of 30 Å is introduced along the interlayer direction to minimize periodic interactions. The exchange-correlation effects are described using the Perdew-Burke-Ernzerhof (PBE) functional within the generalized gradient approximation (GGA) framework [40, 41]. Additionally, the more accurate Heyd-Scuseria-Ernzerhof hybrid functional method (HSE06) is employed to investigate changes in the SBH [42]. The convergence criteria for electronic energy and Hellman-Feynman forces are set to $10^{-6}$ eV and 0.001 eV/Å, respectively. A Gamma-centered $k$-mesh of $12 \times 12 \times 1$ grid is used for static calculations, ensuring precise energy estimation by preserving full lattice symmetry. Spin-orbit coupling (SOC) is included in the first-principles calculations to assess the magnetic anisotropy energy (MAE).

Transport properties of the $MAX_3$-based vdW tunnel junctions are simulated using the Atomistix ToolKit (ATK) package [43,44]. A double-zeta polarized (DZP) atomic-orbital basis is applied for all atoms, with an energy cutoff of 100 Hartree. A $k$-point grid of $1 \times 5 \times 200$ is used to sample the device region and the electron temperature is set to 300 K. The tunneling conductance under the equilibrium state can be obtained using the following equation [45,46]:

$$\mathcal{G}(E) = \frac{e^2}{h} \sum_k T(k, E), \tag{1}$$

where $e$ is the electron charge, $h$ is the Planck's constant, and $T(k,\ E)$ is the transmission coefficient at energy $E$ for a specific wave vector $k$. The current-voltage $I$-$V$ characteristics under non-equilibrium conditions are determined using the Hanasuer-Buttiker formula:

$$I = \frac{e}{h} \int T(E, V)[f(E - \mu_L) - f(E - \mu_R)]\mathrm{d}E, \tag{2}$$

where $T(E, V)$ is the sum of $T(k, E)$ in first Brillouin zone under the applied bias voltage $V$, $f$ is the Fermi distribution function, and $\mu$ is the chemical potentials.

## 3 Results and discussion

As illustrated in Figures 1(a) and (b), both $MnSiSe_3$ and $ZnPSe_3$ monolayers exhibit the symmetry of the space group $P\bar{3}1m$ (Table S1, Figures S2–S5). We begin by constructing a bilayer $MnSiSe_3$ structure. Assuming that the $c$-axis aligns with the direction of the interlayer, the second layer can be generated by applying the operator $\tau_c\hat{O}$ to the first layer. Here, $\tau_c$ represents the out-of-plane translation operator, corresponding to the vertical separation between the two metallic honeycomb layers. The transformation operator $\hat{O} = \{O|\tau_0\}$ consists of an in-plane translational component $\tau_0$ (expressed in fractional coordinates) and a rotational component $O$. We explore several configurations where the rotational component $O$ can be either $E$ (the identity element) or $m_z$ (mirror symmetry about the $ab$-plane), and the translational component $\tau_0$ can be $G$ (the identity element) or any point within the unit cell (see Figure S1(a) for details on high-symmetry translation points). We defined $\tau_0'$ as the spatial inversion symmetry operator of $\tau_0$. Each combination allows us to investigate different configurations of bilayer $MnSiSe_3$. For the case of $MnSiSe_3/ZnPSe_3$ heterostructure, one layer of Mn and Si can be replaced with Zn and P atoms, respectively (similarly for $NiSiSe_3/ZnPSe_3$, $MnGeSe_3/ZnAsSe_3$, and $MnSiS_3/ZnPS_3$). The lattice mismatch in these

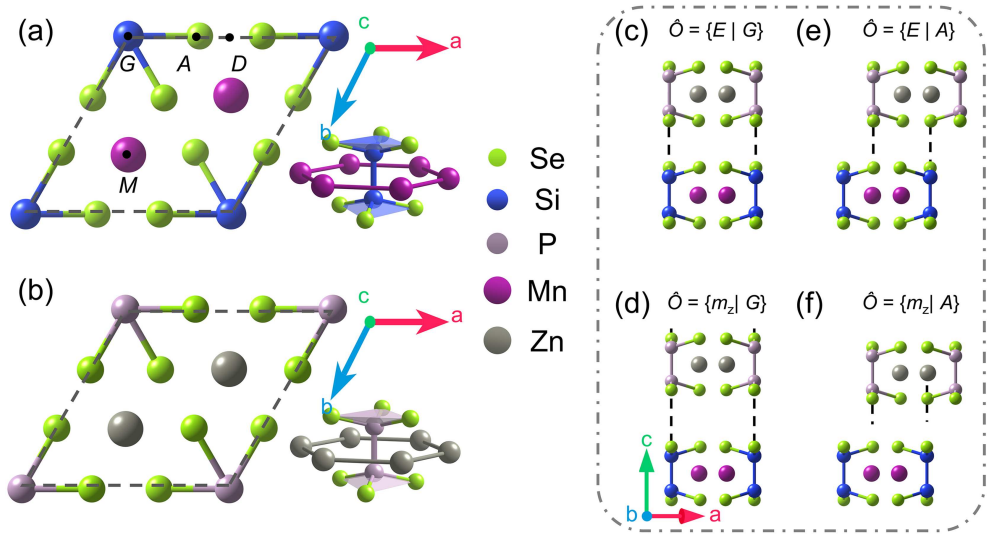


**Figure 1** (Color online) Top view of the unit cell of (a) $MnSiSe_3$ and (b) $ZnPSe_3$ monolayers, where the bipyramid structure $[(P_2Se_6)^{4-}$ and $(Si_2Se_6)^{6-}]$ is embedded within a hexagonal honeycomb lattice comprised of transition metal atoms. (c)–(f) Side views of $MnSiSe_3/ZnPSe_3$ heterostructure obtained using different operations.

**Table 1** Schottky barrier heights (SBH, in the unit of meV) for each structure. The transformation operator has been simplified (e.g., $m_zG = \{m_z|G\}$).

| Configuration and SBH | $m_zG$ | $m_zA$ | $m_zD$ | $m_zM$ |
|---|---|---|---|---|
| $MnSiSe_3/ZnPSe_3$ | 60.7 | 3.1 | 5.5 | 19.1 |
| $NiSiSe_3/ZnPSe_3$ | 101.2 | 25.6 | 28.3 | 49.9 |
| $MnGeSe_3/ZnAsSe_3$ | 238.5 | 73.8 | 101.8 | 121.9 |
| $MnSiS_3/ZnPS_3$ | 141.1 | 74.6 | 93.5 | 82.6 |

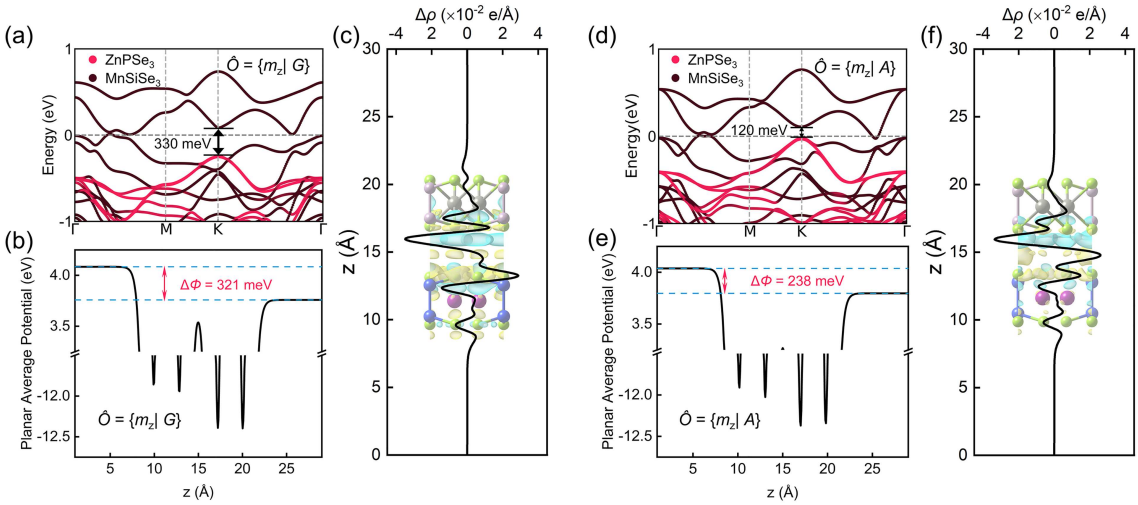


**Figure 2** (Color online) The layer-resolved HSE06 band structure, the plane-averaged electrostatic potential, the plane-averaged differential charge density, and the corresponding three-dimensional differential charge density of $MnSiSe_3/ZnPSe_3$ obtained by using the operations (a)–(c) $\hat{O} = \{m_z|G\}$ and (d)–(f) $\hat{O} = \{m_z|A\}$.

heterostructures is minimal due to the small differences in their in-plane lattice constants, ensuring a flat interface (Tables S2–S5).

The band structures of these heterostructures, computed using the PBE method under various transformation operators, are shown in Figures S7–S10. The SBHs are provided in Table 1. Notably, the SBH reaches its maximum under the operation $\hat{O} = \{m_z|G\}$ and its minimum under $\hat{O} = \{m_z|A\}$. In the absence of mirror operations, the SBH remains nearly unchanged with respect to the sliding mode (Tables S6 and S7 for details).

Taking the $MnSiSe_3/ZnPSe_3$ heterostructure as an example, the SBH under $\hat{O} = \{m_z|G\}$ is 60 meV, while under

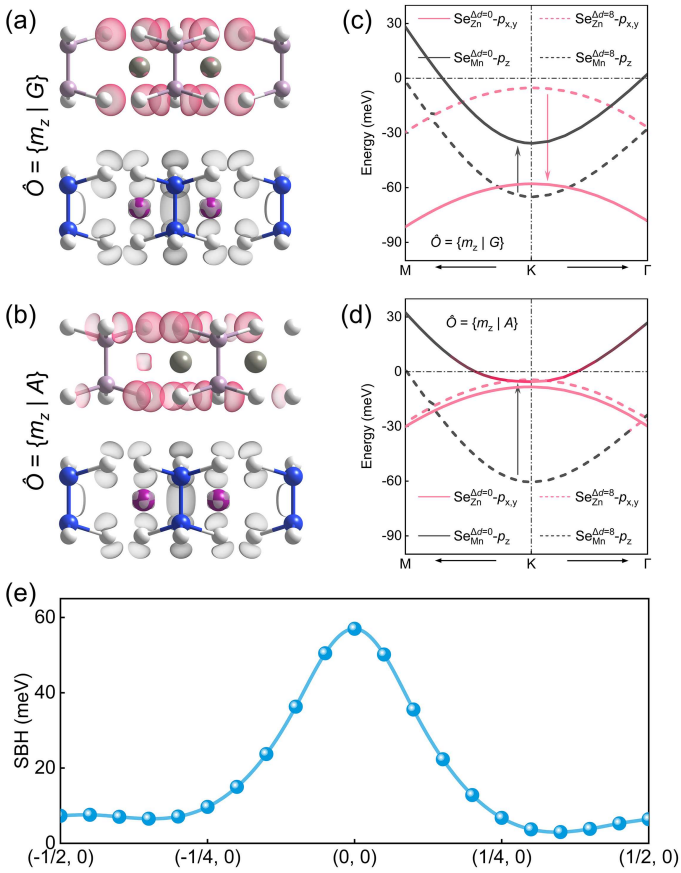


**Figure 3** (Color online) Partial charge density at the K point near the Fermi level of structures (a) $\hat{O} = \{m_z|G\}$ and (b) $\hat{O} = \{m_z|A\}$. The variation in band structure with changing interlayer distances ($\Delta d = 0,\ 8$ Å) for configurations (c) $\hat{O} = \{m_z|G\}$ and (d) $\hat{O} = \{m_z|A\}$, focusing specifically on the scenario at the K point close to the Fermi level. (e) The variation of the Schottky barrier following a shift of the top layer by one lattice period along the zigzag direction.

$\hat{O} = \{m_z|A\}$, it decreases to 3 meV. This trend is further confirmed using the more accurate HSE06 method, which shows a reduction from 240 to 20 meV (refer to Figures 2(a) and (d)). The charge transfer mechanism between the two layers of selenium (Se) atoms in different configurations, such as $\hat{O} = \{m_z|G\}$ and $\hat{O} = \{m_z|A\}$, plays a crucial role in modulation the barrier. As depicted in Figures 2(b) and (e), the internal electric fields in these configurations vary significantly, with $\hat{O} = \{m_z|G\}$ exhibiting a more robust field compared to $\hat{O} = \{m_z|A\}$. This indicates more pronounced charge transfer in $\hat{O} = \{m_z|A\}$, leading to a greater downward shift of the $ZnPSe_3$ energy bands and the formation of a $p$-type Schottky barrier at the K point.

Additionally, Figures 2(c) and (f) depict the plane-averaged differential charge density, highlighting variations in charge transfer zones. In the $\hat{O} = \{m_z|G\}$ configuration, the transferred charge is localized around the Se atoms of $MnSiSe_3$, whereas in the $\hat{O} = \{m_z|A\}$ configuration, it is primarily localized within the interlayer gap, leading to variations in the Schottky barrier thickness. Analysis of the projected band structure reveals that the energy bands near the Fermi level at the K point consist of two components (Figure S11): the $p_z$ orbital of Se atoms in the $MnSiSe_3$ layer ($Se^{Mn}$-$p_z$) and the $p_{x,y}$ orbitals of Se atoms in the $ZnPSe_3$ layer ($Se^{Zn}$-$p_{x,y}$) (similarly for $NiSiSe_3/ZnPSe_3$, $MnGeSe_3/ZnAsSe_3$, and $MnSiS_3/ZnPS_3$, Figures S12–S14). A clearer depiction is provided by the partial charge density plot, as illustrated in Figures 3(a) and (b), where both in-plane $p_{x,y}$ orbitals and out-of-plane $p_z$ orbital are visible.

To further elucidate the charge transfer, we calculated the band structure as a function of interlayer distance. We define $\Delta d = d - d_0$, where $d$ and $d_0$ denote the manually adjusted and optimized interlayer distances, respectively. The value of $\Delta d$ ranges from 0 to 9 Å. For large interlayer distances ($\Delta d$ =8, 9 Å, Figure S15), the band structures show negligible differences, indicating that the heterostructure behaves as two independent monolayers with minimal interaction. As the interlayer distance decreases, different configurations exhibit distinct trends ($\Delta d = 0,\ 8$ Å; refer to Figures 3(c) and (d)). In the $\hat{O} = \{m_z|A\}$ configuration, only the energy band contributed by $Se^{Mn}$-$p_z$ shifts upward, while the energy band contributed by $Se^{Zn}$-$p_{x,y}$ remains unchanged. In the $\hat{O} = \{m_z|G\}$ configuration, the

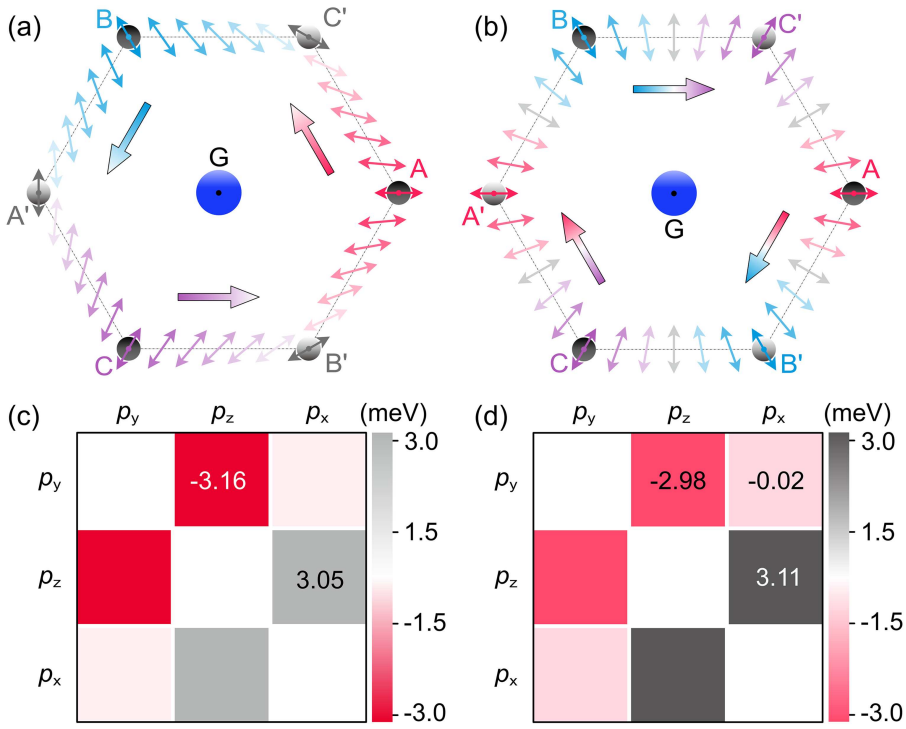


**Figure 4** (Color online) Variation of the magnetic easy axis in (a) $MnSiSe_3/ZnPSe_3$ heterostructures and (b) mirrored-bilayer $MnSiSe_3$ with the designed sliding path. Blue circles indicate the positions of Si atoms, while the Se atoms in the bipyramid structure are color-coded for clarity, with the upper layer shown in black and the lower layer in white. The translation points are presented in the form of fractional coordinates: $A$ (1/3, 0), $B$ (0, 1/3), $C$ (−1/3, −1/3), $A'$ (−1/3, 0), $B'$ (0, −1/3), $C'$ (−1/3, −1/3). The orbital-resolved SOC energy difference of selenium atoms in $MnSiSe_3/ZnPSe_3$ heterostructures, calculated using the operators (c) $\hat{O} = \{m_z|A\}$ and (d) $\hat{O} = \{m_z|A'\}$.

energy band contributed by $Se^{Mn}$-$p_z$ shifts upward, while the energy band contributed by $Se^{Zn}$-$p_{x,y}$ shifts downward, leading to an increase in the Schottky barrier.

The upward and downward shifts of the energy bands signify electron transfer. The barrier alteration is ultimately ascribed to the charge transfer between $Se^{Zn}$-$p_z$ and $Se^{Zn}$-$p_{x,y}$ under $\hat{O} = \{m_z|G\}$, a phenomenon less evident under $\hat{O} = \{m_z|A\}$ or other operations. Quantifying interlayer charge transfer in the heterostructure is essential for understanding the underlying mechanism. Bader charge analysis confirms the proposed charge transfer mode (Tables S2–S5), demonstrating maximum charge transfer under the $\hat{O} = \{m_z|G\}$ operation and minimum transfer under $\hat{O} = \{m_z|A\}$. This trend remains consistent across all four heterostructures studied. Figure 3(e) illustrates the variation of the Schottky barrier as the top material shifts by one lattice period along the zigzag direction of the metallic honeycomb lattice ($D' \to G \to D$). Notably, sliding magnetism is achievable in these heterostructures, as suggested in our prior research [33]. Sliding along a specified path enables 180-degree control of in-plane magnetization, differing slightly from the behavior observed in mirrored-bilayer $MnSiSe_3$. For $MnSiSe_3/ZnPSe_3$, reversing the magnetic easy axis requires a full cycle along the path ($A \to C' \to B \to A' \to C \to B' \to A$, Figures 4(a) and S21), whereas in mirrored-bilayer $MnSiSe_3$, only half a cycle is needed ($A \to B' \to C \to A'$, see Figure 4(b)).

This discrepancy arises from a reduction in the system's symmetry. The $MnSiSe_3/ZnPSe_3$ heterostructure, classified under the $C_{3v}$ point group using $\hat{O} = \{m_z|G\}$, exhibits different symmetry compared to bilayer $MnSiSe_3$, which belongs to the $D_{3h}$ point group under the same operation. As illustrated in Figures 4(a) and (b), the translation points $A$ and $A'$ are equivalent in the bilayer case but not in the heterostructure (similarly for $B/B'$ points and $C/C'$ points). The MAE for other heterostructures has also been calculated (Figures S16–S18). The essence of sliding magnetism lies in the spin-orbit coupling (SOC) interactions influenced by different lattice symmetries, which can be evaluated using second-order perturbation theory

$$E^{\varphi}_{\tau_0,O} = \frac{|\langle o|\hat{H}_{\mathrm{SOC}}|u\rangle|^2}{\varepsilon_o - \varepsilon_u}, \tag{3}$$

where $\phi$ is the azimuth angle of the magnetic moment ($\phi = 0°$ and $90°$ present the magnetic moment point to the $x$ and $y$ directions, respectively), $|o\rangle$ ($|u\rangle$), $\varepsilon_o$ ($\varepsilon_u$), stand for the occupied (unoccupied) states and the corresponding energies. The alteration of the magnetic easy axis is primarily driven by the Se atom within the $MnSiSe_3$ layer

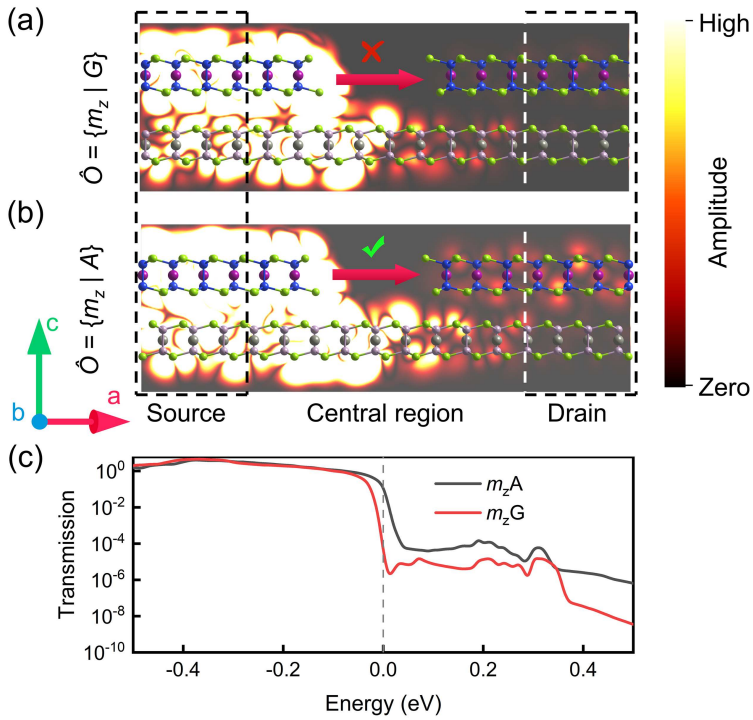


**Figure 5** (Color online) Side views of tunnel junction based on $MnSiSe_3/ZnPSe_3$ heterostructures obtained using the operations (a) $\hat{O} = \{m_z|G\}$ and (b) $\hat{O} = \{m_z|A\}$, where the scattering states at the Fermi level are embedded in the background. (c) The transmission spectrums of $MnSiSe_3/ZnPSe_3$-based tunnel junction at the equilibrium state.

(Figure S20, using $MnSiSe_3/ZnPSe_3$ as an example; a similar situation occurs in other heterostructures, as the energy bands near the Fermi level are also predominantly contributed by chalcogen elements).

The orbital-resolved SOC energy differences of $MnSiSe_3/ZnPSe_3$ are analyzed for two cases: $\hat{O} = \{m_z|A\}$ $(E^0_{m_z,A} - E^{90}_{m_z,A})$ and $\hat{O} = \{m_z|A'\}$ $(E^0_{m_z,A'} - E^{90}_{m_z,A'})$. In the case of $\hat{O} = \{m_z|A\}$ (see Figure 4(c)), the coupling between the $p_y$ and $p_z$ states ($\langle p_y|\hat{H}_{\rm SOC}|p_z\rangle \sim \langle S_x\rangle$), which predominantly contribute to the magnetic easy axis along the $x$-direction, exerts a more significant influence than the coupling between the $p_x$ and $p_z$ states ($\langle p_x|\hat{H}_{\rm SOC}|p_z\rangle \sim \langle S_y\rangle$), the main contributors to the magnetic easy axis along the $y$-direction. Figure 4(d) illustrates that the situation is completely reversed for $\hat{O} = \{m_z|A'\}$. The calculated magnetic moment for selenium atoms is around 0.147 $\mu_B$ in all cases; thus, the alteration of magnetic easy axis can be attributed to the variations in the energy difference between the $p_z$ and $p_x$, $p_y$ states at various sliding positions, as indicated in (3).

Given the metal-semiconductor composition of our system, we investigated the magnetic proximity effect upon heterostructure formation. Our analysis of chalcogenide atoms in the semiconductor layer reveals induced magnetic moments on the order of $10^{-3}$ $\mu_B$ (Figure S6), indicating a negligible magnetic proximity effect. Notably, we find no direct correlation between charge transfer and easy axis orientation. While the $\hat{O} = \{m_z|G\}$ operation produces maximal charge transfer but minimal easy axis variation (Figure S19(b)), the $\hat{O} = \{m_z|A\}$ operation yields minimal charge transfer yet maximal easy axis modification (Figure S19(d)). Instead, our results demonstrate that the magnetic easy axis is predominantly governed by system symmetry. Under $\hat{O} = \{m_z|G\}$ operation ($D_{3h}$ symmetry), the magnetic easy axis exhibits threefold rotational symmetry, whereas under $\hat{O} = \{m_z|A\}$ operation ($C_{\rm s}$ symmetry), it displays corresponding mirror symmetry.

Accordingly, the Schottky barrier and the magnetic easy axis direction of these heterostructures can be effectively modulated through sliding. The maximum sliding energy barrier in this heterostructure is approximately 40 meV/f.u. (Figure S1(a)), which is lower than that of other control methods, such as chemical doping (binding energy of core levels increases by 0.7 eV in $WS_2$) [25], applying external electric fields (requiring 1.7 V/nm) [26], and polarization switching (~1 eV/f.u. for $Sc_2CO_2$) [28]. We then investigate whether such changes can improve device performance.

As depicted in Figures 5(a) and (b), a tunnel junction is constructed with the $MnSiSe_3/ZnPSe_3$ heterostructure as the electrode and an insulating $ZnPSe_3$ monolayer. The zigzag direction of the metallic honeycomb lattice is selected as the transport direction. According to the first-principles calculations, the structure obtained using $\hat{O} = \{m_z|G\}$ exhibits a higher Schottky barrier, corresponding to the device's high-resistance (HR) state, while

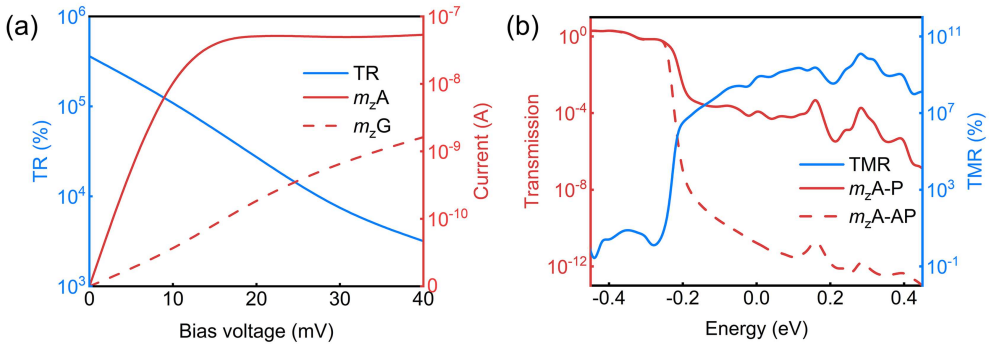


**Figure 6** (Color online) (a) The TR ratio (blue line), current of $m_zA$ (red line), and $m_zG$ (red dashed line) configuration vs. bias voltage of $MnSiSe_3/ZnPSe_3$ vdW tunnel junction. (b) The TMR ratio (blue line), the transmission of $m_zA$-P (red line), and $m_zA$-AP (red dashed line) configuration of $MnSiSe_3/ZnPSe_3$ vdW tunnel junction.

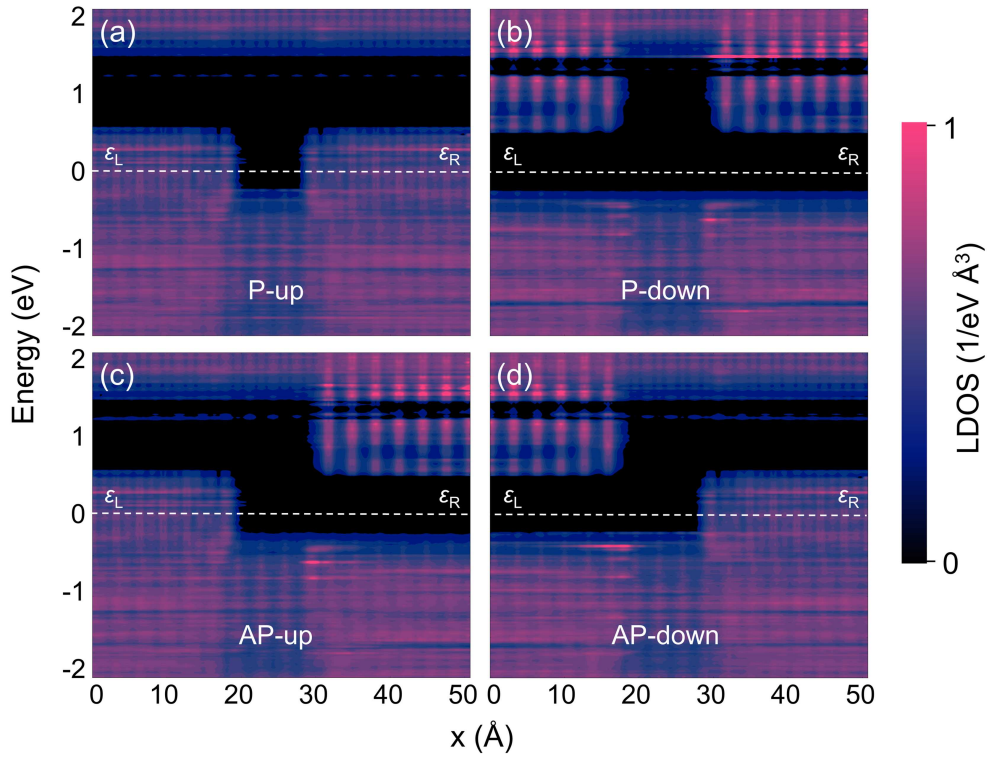


**Figure 7** (Color online) In the case of $MnSiSe_3/ZnPSe_3$ vdW tunnel junction, the spin-resolved LDOS under (a) and (b) parallel, (c) and (d) anti-parallel configuration.

the structure obtained using $\hat{O} = \{m_z|A\}$ corresponds to a low-resistance (LR) state. The TR ratios are defined as $\mathrm{TR} = |\mathcal{G}_{m_zA} - \mathcal{G}_{m_zG}|/\mathcal{G}_{m_zG}$ and $\mathrm{TR} = |I_{m_zA} - I_{m_zG}|/I_{m_zG}$ for the equilibrium and none-equilibrium states, respectively.

At zero bias, the system reaches a TR value of $6 \times 10^5$, as shown in Figures 5(c) and 6(a). The scattering states are analyzed to intuitively demonstrate the sliding-dependent Schottky barrier in the $MnSiSe_3/ZnPSe_3$-based vdW tunnel junction (see embedded scattering states in Figures 5(a) and (b)). In the HR state ($\hat{O} = \{m_z|G\}$), a higher and wider barrier at the interface localizes the scattering states, preventing electron transport between the electrodes. Conversely, shifting the heterostructure to the $\hat{O} = \{m_z|A\}$ state reduces the barrier, facilitating the distribution of scattering states throughout the transmission channel and enabling efficient electron movement between the source and drain electrodes. Figure 6(a) also presents the transport properties of the $MnSiSe_3/ZnPSe_3$-based vdW tunnel junction in a non-equilibrium state. As the bias increases, TR decreases because the current in the HR state varies more significantly with bias than in the LR state.

Moreover, sliding magnetism enables the realization of the TMR effect within the same device (detailed spin-dependent transmission spectra of each device are provided in Figure S25). By moving the heterostructure along

**Table 2** Performance of the tunnel junctions based on $MAX_3$ heterostructures.

| Systems | TR (%) | TMR (%) |
|---|---|---|
| $MnSiSe_3/ZnPSe_3$ | $5.9 \times 10^5$ | $1.1 \times 10^{10}$ |
| $NiSiSe_3/ZnPSe_3$ | $9.5 \times 10^2$ | $7.1 \times 10^9$ |
| $MnGeSe_3/ZnAsSe_3$ | $4.1 \times 10^4$ | $2.9 \times 10^9$ |
| $MnSiS_3/ZnPS_3$ | $5.1 \times 10^2$ | $5.7 \times 10^{10}$ |

the designed path ($A \to C' \to B \to A' \to C \to B' \to A$), parallel (P) and anti-parallel (AP) magnetization configurations can be achieved, resulting in a TMR ratio up to $10^{10}$% (see Figure 6(b), TMR $= |\mathcal{G}_{\rm P} - \mathcal{G}_{\rm AP}|/\mathcal{G}_{\rm AP}$. Analysis of the local density of states (LDOS) reveals that the high TMR ratio is due to the single-spin channel characteristics of $MnSiSe_3$ near the Fermi level (see Figure 7): in the parallel magnetization configuration (P), two conduction channels are present in both the left and right electrodes for spin-up electrons (Figure 7(a)), yielding a maximum transmission coefficient ($T_\uparrow$) (purple line in Figure S25(a)). In contrast, the P configuration exhibits no conduction channels for spin-down electrons (Figure 7(b)), resulting in an absence of states connecting the electrodes across the device and a minimal transmission coefficient ($T_\downarrow$) (black line in Figure S25(a)). In the antiparallel magnetization configuration (AP), only one conduction channel exists for either spin-up or spin-down electrons (Figures 7(c) and (d)), leading to an intermediate transmission coefficient (blue and red lines in Figure S25(a)). The performance of the tunnel junctions based on $MAX_3$ heterostructures is summarized in Table 2, showing remarkable performance (detailed transmission spectra of each device are provided in Figures S22 and S23).

## 4 Conclusion

In summary, we investigate the interfacial and transport properties of $MAX_3$-based heterostructures under controlled sliding operations ($\hat{O} = \{O|\tau_0\}$) using density functional theory. Our findings reveal that sliding enables precise modulation of both the SBH and the magnetic easy-axis orientation in these heterostructures. Capitalizing on this mechanism, we design $MAX_3$-based tunneling junctions to demonstrate the efficacy of the sliding strategy. By tuning the SBH, we achieve a TR ratio enhancement of up to $10^5$%, while optimizing the magnetic easy axis yields a TMR ratio as high as $10^{10}$%. This study establishes a low-energy, sliding-driven approach for tailoring quantum transport in 2D vdW heterostructures, offering a promising pathway for designing high-efficiency, reconfigurable memory devices.

**Acknowledgements** This work was supported by National Natural Science Foundation of China (Grant No. 12474226).

**Supporting information** Figures S1–S30, Tables S1–S8. The supporting information is available online at info.scichina.com and link.springer.com. The supporting materials are published as submitted, without typesetting or editing. The responsibility for scientific accuracy and content remains entirely with the authors.

**References**

1 Wolf S A, Awschalom D D, Buhrman R A, et al. Spintronics: a spin-based electronics vision for the future. Science, 2001, 294: 1488–1495
2 Tsymbal E Y, Kohlstedt H. Tunneling across a ferroelectric. Science, 2006, 313: 181–183
3 Chanthbouala A, Crassous A, Garcia V, et al. Solid-state memories based on ferroelectric tunnel junctions. Nat Nanotech, 2012, 7: 101–104
4 Qiu H, Yu Z H, Zhao T G, et al. Two-dimensional materials for future information technology: status and prospects. Sci China Inf Sci, 2024, 67: 160400
5 Yu L, Lee Y H, Ling X, et al. Graphene/$MoS_2$ hybrid technology for large-scale two-dimensional electronics. Nano Lett, 2014, 14: 3055–3063
6 Novoselov K S, Mishchenko A, Carvalho A, et al. 2D materials and van der Waals heterostructures. Science, 2016, 353: aac9439
7 Seixas L, Rodin A S, Carvalho A, et al. Multiferroic two-dimensional materials. Phys Rev Lett, 2016, 116: 206803
8 Shen T, Ren J C, Liu X, et al. van der Waals stacking induced transition from Schottky to Ohmic contacts: 2D metals on multilayer InSe. J Am Chem Soc, 2019, 141: 3110–3115
9 Gong C, Kim E M, Wang Y, et al. Multiferroicity in atomic van der Waals heterostructures. Nat Commun, 2019, 10: 2657
10 Liu Y, Duan X, Shin H J, et al. Promises and prospects of two-dimensional transistors. Nature, 2021, 591: 43–53
11 Su Y, Li X, Zhu M, et al. Van der Waals multiferroic tunnel junctions. Nano Lett, 2021, 21: 175–181
12 Pendurthi R, Sakib N U, Sadaf M U K, et al. Monolithic three-dimensional integration of complementary two-dimensional field-effect transistors. Nat Nanotechnol, 2024, 19: 970–977
13 Xu D, Tan J, Ge M, et al. Multifunctional near-infrared polarized photodetector driven by the anisotropic photogalvanic effect in a two-dimensional MnSSe/$TaIr_4$/MnSSe magnetic tunnel junction. Phys Rev Appl, 2024, 22: 054042

14 Gong C, Colombo L, Wallace R M, et al. The unusual mechanism of partial Fermi level pinning at Metal-$MoS_2$ interfaces. Nano Lett, 2014, 14: 1714–1720

15 Kim C, Moon I, Lee D, et al. Fermi level pinning at electrical metal contacts of monolayer molybdenum dichalcogenides. ACS Nano, 2017, 11: 1588–1596

16 Liu Y, Guo J, Zhu E, et al. Approaching the Schottky-Mott limit in van der Waals metal-semiconductor junctions. Nature, 2018, 557: 696–700

17 Yan Z, Li Z, Han Y, et al. Giant tunneling magnetoresistance and electroresistance in $\alpha$-$In_2Se_3$-based van der Waals multiferroic tunnel junctions. Phys Rev B, 2022, 105: 075423

18 Wang X, Hu Y, Kim S Y, et al. Origins of Fermi level pinning for Ni and Ag metal contacts on tungsten dichalcogenides. ACS Nano, 2023, 17: 20353–20365

19 Yu X, Zhang X, Wang J. Fully electrically controlled van der Waals multiferroic tunnel junctions. ACS Nano, 2023, 17: 25348–25356

20 Lin X, Yang W, Wang K L, et al. Two-dimensional spintronics for low-power electronics. Nat Electron, 2019, 2: 274–283

21 Zhang L, Zhou J, Li H, et al. Recent progress and challenges in magnetic tunnel junctions with 2D materials for spintronic applications. Appl Phys Rev, 2021, 8: 021308

22 Yang H, Valenzuela S O, Chshiev M, et al. Two-dimensional materials prospects for non-volatile spintronic memories. Nature, 2022, 606: 663–673

23 Wang Y K, Ge M, Tan J N, et al. Dipole-moment modulation of photovoltaic and photoresponse properties in 2H-MoSSe/$MoS_2$ van der Waals heterojunctions under electric field. Sci China Inf Sci, 2025, 68: 159402

24 Yang W, Xu Y B, Li S, et al. Large and multistate magnetoresistance in 2D van der Waals multiferroic tunnel junctions. Sci China Mater, 2025, 68: 1622–1629

25 Yang L, Majumdar K, Liu H, et al. Chloride molecular doping technique on 2D Materials: $WS_2$ and $MoS_2$. Nano Lett, 2014, 14: 6275–6280

26 Padilha J E, Fazzio A, da Silva A J R. van der Waals heterostructure of phosphorene and graphene: tuning the Schottky barrier and doping by electrostatic gating. Phys Rev Lett, 2015, 114: 066803

27 Hu H, Ouyang G. Interface-induced transition from Schottky-to-Ohmic contact in $Sc_2CO_2$-based multiferroic heterojunctions. Phys Chem Chem Phys, 2021, 23: 827–833

28 Liu G, Ke S H. Ferroelectric control of the semiconductor-metal transition in two-dimensional $MSi_2P_4/Sc_2CO_2$ (M = Mo, W) van der Waals heterostructures and application to nonvolatile memory devices. Phys Rev Appl, 2024, 21: 044033

29 Yu Z, Huang X, Bian J, et al. On-device pressure-tunable moving Schottky contacts. Nano Lett, 2024, 24: 12179–12187

30 Li L, Wu M. Binary compound bilayer and multilayer with vertical polarizations: two-dimensional ferroelectrics, multiferroics, and nanogenerators. ACS Nano, 2017, 11: 6382–6388

31 Yasuda K, Wang X, Watanabe K, et al. Stacking-engineered ferroelectricity in bilayer boron nitride. Science, 2021, 372: 1458–1462

32 Ji J, Yu G, Xu C, et al. General theory for bilayer stacking ferroelectricity. Phys Rev Lett, 2023, 130: 146801

33 Tan J, Xu D, Ge M, et al. Sliding ferromagnetism in bilayer $MnSiSe_3$ and its application to spintronics. Phys Rev B, 2024, 110: 125402

34 Pan B, Zhou P, Lyu P, et al. General stacking theory for altermagnetism in bilayer systems. Phys Rev Lett, 2024, 133: 166701

35 Chittari B L, Park Y, Lee D, et al. Electronic and magnetic properties of single-layer $MPX_3$ metal phosphorous trichalcogenides. Phys Rev B, 2016, 94: 184428

36 Chittari B L, Lee D, Banerjee N, et al. Carrier- and strain-tunable intrinsic magnetism in two-dimensional $MAX_3$ transition metal chalcogenides. Phys Rev B, 2020, 101: 085415

37 Hohenberg P, Kohn W. Inhomogeneous electron gas. Phys Rev, 1964, 136: B864–B871

38 Blöchl P E. Projector augmented-wave method. Phys Rev B, 1994, 50: 17953–17979

39 Grimme S, Antony J, Ehrlich S, et al. A consistent and accurate ab initio parametrization of density functional dispersion correction (DFT-D) for the 94 elements H-Pu. J Chem Phys, 2010, 132: 154104

40 Kresse G, Furthmüller J. Efficiency of ab-initio total energy calculations for metals and semiconductors using a plane-wave basis set. Comput Mater Sci, 1996, 6: 15–50

41 Perdew J P, Burke K, Ernzerhof M. Generalized gradient approximation made simple. Phys Rev Lett, 1996, 77: 3865–3868

42 Heyd J, Scuseria G E, Ernzerhof M. Hybrid functionals based on a screened Coulomb potential. J Chem Phys, 2003, 118: 8207–8215

43 Smidstrup S, Markussen T, Vancraeyveld P, et al. QuantumATK: an integrated platform of electronic and atomic-scale modelling tools. J Phys-Condens Matter, 2019, 32: 015901

44 Gong M, Xie D, Tian Y, et al. Unraveling the role of interfacial interactions in electrical contacts of atomically thin transition-metal dichalcogenides. ACS Nano, 2024, 19: 4718–4730

45 Meir Y, Wingreen N S. Landauer formula for the current through an interacting electron region. Phys Rev Lett, 1992, 68: 2512–2515

46 Liu D, Liu Z, Zhu J, et al. Hydrogen-bonding enables two-dimensional metal/semiconductor tunable contacts approaching the quantum limit and the modified Schottky-Mott limit simultaneously. Mater Horiz, 2023, 10: 5621–5632